THE JOURNAL OF PHYSICAL CHEMISTRY C

Article

Cite This: J. Phys. Chem. C 2018, 122, 14996−15009

pubs.acs.org/JPCC

Understanding Chemical Bonding in Alloys and the Representation in Atomistic Simulations

Juan Liu,[†] Emrys Tennessen,[‡] Jianwei Miao,[§,∥] Yu Huang,[∥,⊥] James M. Rondinelli,[‡] and Hendrik Heinz*[,†]

[†]Department of Chemical and Biological Engineering, University of Colorado at Boulder, Boulder, Colorado 80309, United States

[‡]Department of Materials Science and Engineering, Northwestern University, Evanston, Illinois 60208, United States

[§]Department of Physics and Astronomy, [∥]California NanoSystems Institute, and [⊥]Department of Materials Science and Engineering, University of California, Los Angeles, California 90095, United States

Supporting Information

ABSTRACT: Alloys are widely used in catalysts and structural materials. The nature of chemical bonding and the origin of alloy formation energies, defect energies, and interfacial properties have not been well understood to date but are critical to material performance. In this contribution, we explain the polar nature of chemical bonding and an implementation in classical and reactive atomistic simulations to understand such properties more quantitatively. Electronegativity differences between metal atoms lead to polar bonding, and exothermic alloy formation energies are related to charge transfer between the different elements. These differences can be quantified by atomic charges using pairwise charge increments, determined by matching the computed alloy formation energy to experimentally measured alloy formation energies using pair potentials for the pure metals. The polar character of alloys is comparable to organic molecules and partially ionic minerals, for example, AlNi and $AlNi_3$ alloys assume significant atomic charges of ±0.40*e* and +0.60*e*/−0.20*e*, respectively. The subsequent analysis of defect sites and defect energies using force-field-based calculations shows excellent agreement with calculations using density functional theory and embedded atom models (EAM). The formation of vacancy and antisite defects is characterized by a redistribution of charge in the first shell of neighbor atoms in the classical models whereby electroneutrality is maintained and charge increments correlate with differences in electronegativity. The proposed atomic charges represent internal dipole and multipole moments, consistent with existing definitions for organic and inorganic compounds and with the extended Born model (Heinz, H.; Suter, U. W. *J. Phys. Chem. B* **2004,** *108* (47), 18341−18352). The method can be applied to any alloy and has a reproducibility of ±10%. In contrast, quantum mechanical charge schemes remain associated with deviations exceeding ±100%. The atomic charges for alloys provide a simple initial measure for the internal electronic structure, surface adsorption of molecules, and reactivity in catalysis and corrosion. The models are compatible with the Interface force field (IFF), CHARMM, AMBER, OPLS-AA, PCFF, CVFF, and GROMOS for reliable atomistic simulations of alloys and their interfaces with minerals and electrolytes from the nanometer scale to the micrometer scale.

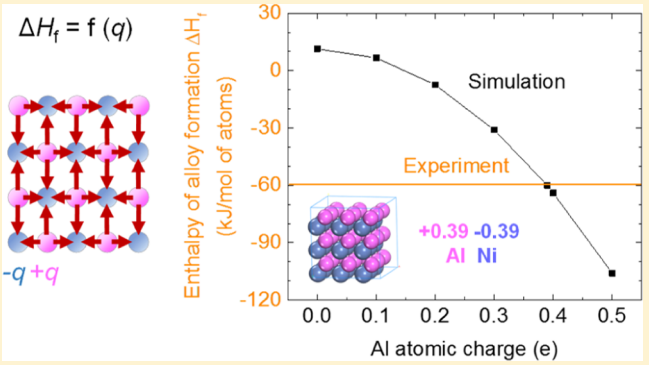

Downloaded via NORTHWESTERN UNIV on October 27, 2018 at 13:05:46 (UTC).
See https://pubs.acs.org/sharingguidelines for options on how to legitimately share published articles.

1. INTRODUCTION

Alloys are used widely in structural materials, catalysts, electrodes, sensors, diagnostics, and therapeutics.[1−5] Understanding the nanoscale and multiscale properties depends on insight into the electronic structure and the nature of chemical bonding, which has been the subject of few studies to date.[6] In particular, no quantitative method to include polarity in alloys in atomistic simulations has been reported. In this contribution, we analyze details of chemical bonding in alloys and introduce a protocol for significantly more accurate all-atom simulations based on pair potentials and reproducible atomic charges.

Pure metals are paradigms for nonpolar bonding between atoms, whereas alloys contain at least two different metals and therefore involve some charge transfer. The discovery of structure−property relationships depends on understanding such heteronuclear bond polarity. The bond polarity correlates with Pauling's electronegativity differences in first-order approximation.[7] However, little is known about chemical bonding alloys[6,8,9] in comparison to the vast available body of knowledge for organic molecules and minerals, and consequently, explanations of interfacial properties and reactivity of alloys remain in their beginnings. Polar versus nonpolar

Received: February 24, 2018
Revised: May 17, 2018
Published: May 31, 2018

© 2018 American Chemical Society

DOI: 10.1021/acs.jpcc.8b01891
J. Phys. Chem. C 2018, 122, 14996−15009

bonding has been largely disregarded in embedded atom model (EAM) and in modified EAM.[10] Assigning physically meaningful atomic charges is also a weakness of first-principles calculations, including density functional theory (DFT), semiempirical quantum mechanics, and advanced coupled cluster calculations.[8,11−15]

Classical atomistic models, in contrast, perform well when using atomic charges that reproduce experimentally measured dipole moments and multipole moments, which is possible with up to 1% accuracy and consistent with electronic structure theory (Figure 1a−e).[8,16−18] For example, when the dipole moment and bond length of a diatomic molecule are known with 1% uncertainty from the experiment, the corresponding atomic charges are defined with 1% accuracy for the force field and, as a result, molecular dynamics simulations of pure compounds, mixtures, and multiphase systems can be carried out in high reliability (Figure 1a,b). This is the founding principle of thermodynamically consistent force fields (Figure 1).[8,19] Dipole moments have been measured and tabulated for thousands of compounds[18] and correlate well with atomic charges derived from experimentally measured electron deformation densities.[8,19,20] On these grounds, we have previously developed a comprehensive method to assign consistent atomic charges also in the absence of exact experimental data, which reaches ±5 to ±10% reproducibility.[8,19,21] In contrast, alternative charges from quantum mechanical simulations exhibit scatter as large as 500% and are hard to use to quantify chemical bonding.[8,11,14,15,19,21−26] The origin of the scatter lies in the quality of the electronic structure calculation (assumptions in DFT and coupled cluster calculations) and in the choice of quantum mechanical charge type (Hirshfeld, Lowdin, Mulliken, Bader, GAPT, CHELPG). Even the different quantum mechanical charge types alone suggest dipole moments that differ up to several multiples for the same diatomic molecule, whereas the dipole moment can be measured anytime in experiment with few percent uncertainty. Such atomic charges have therefore a limited physical justification and are not suitable for predictive atomistic simulations.

These shortcomings of electronic structure calculations may explain that chemical bonding and the role of polarization in alloys have been largely dismissed in the discussion of physical and chemical properties for decades. At the same time, more quantitative understanding and accurate simulation of alloys from atoms to the 1000 nm scale can greatly accelerate the solution of major challenges in chemistry and energy sciences, for example, understanding and designing the activity of nanoscale catalysts, electrode materials, and prevention of corrosion.[27−30]

Electronegativity differences in alloys were first recognized and qualitatively described by Miedema et al.[6] Since then, we are unaware of further quantitative descriptions of polarity; differences in atomic charges were disregarded in classical atomistic models of alloys. Sometime earlier, we reported an initial analysis of polarity for Au−Pd bimetal that indicated significant polarity.[9] In comparison, in organic compounds, the spectrum of covalent bonding, polar covalent bonding, and ionic bonding (such as in carboxylate or ammonium groups) has been carefully examined by orbital theory and is an everyday concept used by synthetic organic, inorganic, and biological chemists (Figure 1a−d).[19,21,31−33] The spectrum of chemical bonding has been implemented in molecular models, and atomic charges consistent with experimentally observable

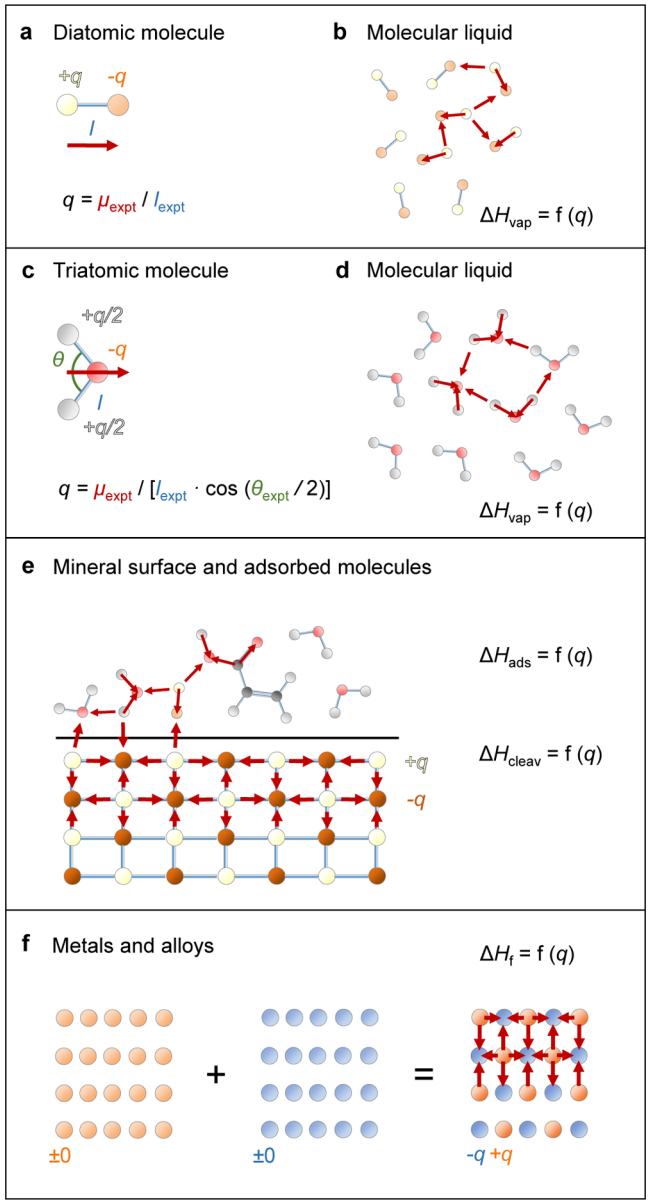

Figure 1. Uniform concept for the assignment of atomic charges in simulations of organic and inorganic compounds including alloys as employed in the IFF (refs 8 and 19). (a) Atomic charges are uniquely defined for diatomic molecules with known dipole moment and bond length from experimental measurements. (b) Atomic charges, in combination with van der Waals interactions, make essential contributions to the vaporization energy ΔH_{vap} of a corresponding molecular liquid or solid, to the surface energy, solubility, and miscibility with other compounds, melting points, boiling points, and chemical reactivity. Dark red arrows illustrate the orientation of intramolecular and intermolecular dipoles that influence these properties. (c) Atomic charges are also uniquely defined in (nonlinear) triatomic molecules with known dipole moment and equilibrium geometry from experimental measurements. (d) Atomic charges affect the same properties of corresponding molecular liquids and solids as in (b). The concept also applies to multiatomic molecules and polymers with repeating functional groups. (e) Atomic charges in minerals are equally defined, including atomic charges from experimentally measured electron deformation densities, dipole moments of inorganic compounds, and the extended Born cycle (ref 8). The atomic charges, in combination with van der Waals and bonded interactions, determine the cleavage energy ΔH_{cleav}, the adsorption energy of organic and inorganic compounds ΔH_{ads}, solubility, defect energies,

DOI: 10.1021/acs.jpcc.8b01891
J. Phys. Chem. C 2018, 122, 14996−15009

Figure 1. continued

melting points, boiling points, and chemical reactivity. Dark red arrows illustrate the orientation of intramolecular, intermolecular, and interfacial dipoles that contribute to these properties. (f) Atomic charges in alloys result from electronegativity differences between the constituting metals and determine the alloy formation energy in combination with van der Waals interactions. This definition and the contribution to the cohesive energy are consistent with other solids and liquids (a−e). Atomic charges in alloys also influence the surface energy, the adsorption energy of organic and inorganic compounds, defect energies, melting points, boiling points, and chemical reactivity (as in (e)).

dipole and multipole moments are routinely included in atomistic simulations of proteins, drugs, DNA, and commercial polymers. We have demonstrated that the same approach works well for inorganic compounds and inorganic−organic interfaces (Figure 1e).[21] For example, silicates, phosphates, and oxides exhibit strong covalent and ionic contributions to bonding. Models with pH specific surface chemistry and consistent atomic charges have improved property predictions to less than 10% uncertainty from up to 500% uncertainty in earlier models and enable full atom mobility as opposed to the need for fixed atoms in prior models.[19,21,22,26,34] On the ionic end of the spectrum, salts such as NaCl can be described by a combination of Coulomb and Lennard-Jones (LJ) interactions in molecular simulations.[8,35] The impact of polarity on solubility, hierarchical assembly, reaction mechanisms, and many other properties is documented knowledge.[17,33,36−38]

Atomic charges suitable for molecular simulations are best derived based on experimentally reproducible dipole moments, or multipole moments, and chemical understanding. When chemical bonding is reasonably represented for a given compound, accurate computations of the geometry (including lattice parameters), the energy (surface energies), as well as the derivatives of the total energy (thermal and mechanical properties) are possible with a limited number of parameters. In contrast, models with less physical bonding descriptions and less suitable atomic charges fail to reproduce such properties simultaneously.[21] Enormous improvements in molecular models are feasible by the quantitative representation of chemical bonding using physically reasoned atomic charges (as opposed to using non-definite, quantum-mechanically derived charges).[8,9,19,22,23,39,40] Once the basic features of bond polarity, crystal structures, and surface properties are translated into atomistic models and force fields, computer simulations of inorganic and organic compounds can predict many properties in high accuracy up to large nanometer scale, including surface properties, hydration, crystal growth, selective adsorption of polymers, biomimetic assembly, folding of macromolecules, and catalytic activity.[41−43]

In this contribution, this concept is extended to alloys (Figure 1f). The starting point is LJ potentials for pristine metals (with or without virtual electrons and polarizability),[44−46] and atomic charges are added upon the formation of alloys. LJ potentials, and extensions for virtual electrons as needed, can reproduce bulk and surface properties of pristine metals in excellent agreement with experiment, explain the binding mechanisms of organic molecules, details of nucleation and shape-directed growth of metal nanostructures, as well as catalytic activities via reactive extensions.[9,21,44,45,47] The models for the alloys, as the models for pure metals,[44] are compatible with common atomistic energy expressions such as the interface force field (IFF), CHARMM, CVFF, DREIDING, AMBER, OPLS-AA, GROMOS/GROMACS, and PCFF and require no added parameters for water, mineral, biomolecular, and polyelectrolyte interfaces. The computational cost is about 10 million (10^7) times lower compared to that of ab initio methods for the same system size, simulation time, and the method reaches comparable accuracy.

The outline of this paper is as follows. Computational details are described in the next section. Then, we present the results and discussion. We first explain our method of quantifying polarity via atomic charges in force fields for compounds across the periodic table, the consistency with related experimental data, and disambiguate the results from ab initio-derived charges. We then correlate experimentally measured alloy formation energies with electronegativity differences, the polarity of bonding, and the representation by atomic charges. Thereafter, as an example, defect formation energies are examined in AlNi and $AlNi_3$ intermetallics with the new model in comparison to EAM and DFT calculations. Changes in the charge distribution in alloys are described as a function of composition and atomic environments, supporting a simple implementation in molecular simulations using pairwise charge increments. The paper ends with conclusions and a survey of potential applications. Additional details and helpful reference data to assign atomic charges for unknown alloys and other compounds are given in the Supporting Information.

2. COMPUTATIONAL DETAILS

Molecular mechanics (MM) and molecular dynamics simulations using the IFF[19,44] were carried out with the programs Discover[48] and LAMMPS,[49] as well as quantum mechanical calculations using DFT (revPBE) with the programs Vienna ab initio simulation package (VASP) and CASTEP.[50,51]

2.1. Molecular Mechanics and Molecular Dynamics Simulations. Models of the unit cells of AlNi (B2 phase)[52,53] and $AlNi_3$ ($L1_2$ phase)[54] were constructed from X-ray data. The size of the super cells was chosen as 3 × 3 × 3 and 2 × 2 × 2 to include a similar small number of atoms and to be able to compare the results of classical force field calculations with those of DFT calculations. We also tested 3 × 3 × 3 super cells for $AlNi_3$, which have identical atomic charges and the same defect energies as the 2 × 2 × 2 super cells with <1% deviation.

The potentials for pure Ni, pure Al, and the two alloys were the unmodified 12-6 LJ parameters for Al and Ni[44] as implemented in the IFF.[19] Atomic charges were added for the simulations of the alloys such that the alloy formation energy known from experiment is reproduced (Figure 4).

Small errors in the alloy lattice parameters of 2−3% were accepted as this study focuses on a proof of concept rather than fully optimized parameters for alloys. Minor changes in the LJ parameters of the metals in the alloys can be made to exactly match the alloy density. Atomic charges for reoptimized LJ parameters change less than 2−3% as well.

The LJ parameters reproduce lattice parameters of the neat metals and particularly surface energies very accurately relative to the experiment (<0.2% and <3% deviation), which is remarkably more accurate than EAM and DFT calculations (<2% and <50%).[46,55] The adsorption of solvents and organic/biological molecules can be computed in quantitative agreement with experiment (about 5−10% deviation) and often more accurately than with DFT calculations.[21,47] Mechanical properties are similar in accuracy to DFT calculations (20%

DOI: 10.1021/acs.jpcc.8b01891
J. Phys. Chem. C 2018, 122, 14996−15009

deviation relative to experiment) and somewhat less accurate than with EAM methods, although additions of virtual electrons have shown promise to exceed the performance of EAM models as well.[45,46]

Calculations of the alloy formation energy involved the supercells of the alloys and small supercells of the metals (Ni and Al) as a reference. The average energies per atom were determined. The difference in energies of the alloy and of the corresponding pure metals, normalized by the total number of atoms, yielded the computed alloy formation energy. Convergence was easy to achieve and better than 0.001 kcal/mol (10^{-4} eV) per atom. Geometry optimization and energy minimization were carried out using the programs Discover in Materials Studio,[48] as well as LAMMPS[49] for about 200 steps at 0 K. The summation of van der Waals interactions involved a cutoff at 1.2 nm and the summation of Coulomb interactions the Ewald method in high accuracy (10^{-6}).

Models of defects were constructed by deletion of atoms (vacancies) or substitution of atoms (antisites). Atomic charges at the defect sites were assigned using charge increments in the first shell of neighbor atoms under consideration of overall electroneutrality, ionization potentials, and electron affinities of the surrounding atoms as described in the results (Section 3.4). Typical charge increments are $\pm 0.05e$ between nearest neighbor Al and Ni atoms and $\pm 0.00e$ between atoms of the same kind. Charge distributions that differ from these or similar justified assumptions were also tested (Section 3.4 and Table S2). Geometry optimization, energy minimization, and recording of the defect energies were carried out by MM in each case. The difference in total equilibrium energies, also termed "raw formation energies", is reported (Figure 5).[53,56,57]

Molecular dynamics simulations were also carried out and verified structural stability of the alloy phases. The simulations used an implementation of the metal/alloy parameters in standard force fields including CHARMM-IFF, CVFF-IFF, and GROMOS-IFF. The simulations can be scaled up to millions of atoms and include mineral, biomolecular, and solvent interfaces without the need to add any further parameters for the interfaces.[19]

2.2. DFT Calculations. Calculations of the formation energy of point defects for NiAl and Ni_3Al were carried out using the VASP. The Perdew–Burke–Ernzerhof functional of the generalized-gradient approximation functionals (GGA–PBE) was employed.[50,58−60] The projector augmented-wave (PAW) potentials were incorporated for the representation of Ni and Al.[61,62] The supercell point defect formation energies were computed according to the methodology outlined by Freysoldt et al.,[51] and the raw defect formation energies are reported as in the force-field-based calculations.

VASP calculations using the GGA–PBE density functional used an energy cutoff of 500 eV, supercells of 54 atoms for NiAl ($3 \times 3 \times 3$ super cell) and 108 atoms for Ni_3Al ($3 \times 3 \times 3$ super cell), *k*-meshes of $6 \times 6 \times 6$ for NiAl and $4 \times 4 \times 4$ for Ni_3Al, and PAW potentials for Ni and Al with valence configurations including 16 electrons and 3 electrons, respectively, leading to converged total energies $<10^{-3}$ eV/atom and pressures $<10^{-4}$ kbar. Reference systems were metallic face-centered cubic (fcc) Ni- and Al-metal unit cells containing four atoms, also converged to a cutoff of 500 eV and *k*-meshes of $12 \times 12 \times 12$. Point defect structures were determined with the appropriate removal/replacement of Ni/Al as well as suitable geometric relaxation until the internal pressure was zero. The reported raw defect formation energies were the result of the difference between pristine and defect-incorporated alloy equilibrium energies.

Charge density difference calculations were carried out for NiAl using the same supercell size and parameters as for the calculation of point defect formation energies. To determine the difference in charge densities, self-consistent calculations using the relaxed point defect supercells were carried out to obtain charge densities. Further, self-consistent calculations of the same supercells with the defect corrected with respect to stoichiometry, and still otherwise maintaining the same atomic positions, were carried out to obtain charge densities. Individual atomic charge densities were obtained for Ni and Al atoms in equivalently sized cells. Using these charge densities, the difference was obtained by subtracting the restored charge density from the original relaxed point defect charge density and then adding the charge density of the individual atom, centered on the point defect location. The series of operations maintained electronic and chemical balance.

Because of a difference in the character of the charge density of a Ni/Al atom in an alloy versus a free atom, the operation reflects the redistribution of electrons in the alloy versus the free atom instead of an atom resting in a pristine alloy. This approximation was made in order to observe changes in charge density on the nearest and next-nearest neighboring atoms to the defect, induced by the defect. The charge density of an atom resting in a pristine alloy would be most accurate; however, it is difficult in DFT to disentangle the charge density contribution of a single Ni/Al atom from the bulk of a pristine alloy.

Further calculations using the revPBE and revPBE sol density functional were carried out in CASTEP using an energy cutoff above 400 eV, leading to convergent results upon geometry optimizations up to 200 steps with flexible cell parameters. The defect energies differ by about 0.5 eV (up to 1 eV in some cases) from results with VASP so that ±0.5 eV can be considered a realistic measure of reliability. Atomic charges in DFT calculations (Mulliken, Hirshfeld, Bader) were computed as part of the computations of defect energies using the same periodic unit cells and showed no significant dependence on the system size.

3. RESULTS AND DISCUSSION

3.1. Purpose and Method of Inclusion of Polarity in Accurate Force Fields. The polarity of compounds can be represented in all-atom force fields by atomic charges. A convergent way to do so is (1) in compliance with experimentally measured dipole moments and multipole moments (Figure 1), (2) in compliance with atomic charges derived from experimentally measured electron deformation densities (which were found to be consistent with dipole moments[8,19,20]), and (3) in compliance with the extended Born model when no direct data are available (Figure 2).[8,19] The extended Born model describes the energy of formation of a given compound in terms of atomization energies, partial ionization energies and electron affinities, electrostatic contributions, and nonpolar contributions to the cohesive energy (steps 1–5 in Figure 2). The assignment of atomic charges using the extended Born model relies on trends in these and other polarity-related properties for structurally and electronically similar compounds across the periodic table. Main criteria to assign relative atomic charges include relative differences in atomization energies, ionization energies, and coordination numbers, as well as differences in melting points, solubility,

DOI: 10.1021/acs.jpcc.8b01891
J. Phys. Chem. C 2018, 122, 14996−15009

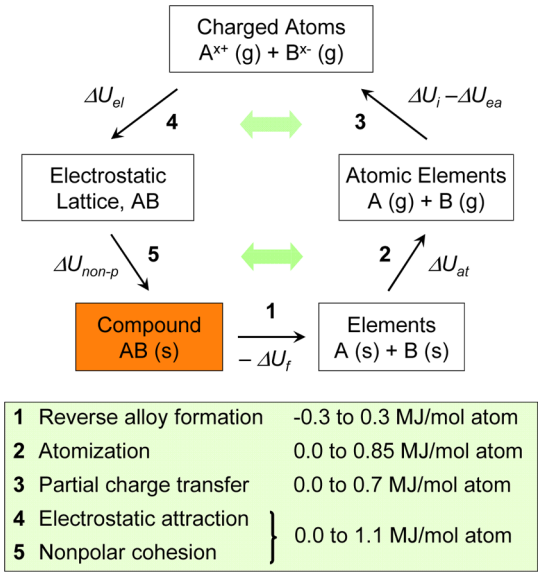

Figure 2. Extended Born model (adapted from ref 8). The model can quantify polar bonding and nonpolar bonding in compounds across the periodic table in a closed thermodynamic cycle. It is depicted here for an alloy represented by metal components A and B (in 1:1 stoichiometry for simplicity). The alloy formation energy ΔU_f (step 1) is described as a process of atomization of the neat metals (step 2), partial ionization and electron affinity of gas-phase atoms (step 3), formation of the solid alloy by electrostatic attraction (step 4), and remaining nonpolar attraction to cohesion (step 5). Ionization can be partial or full, and the cohesive energy is divided into additive electrostatic and nonpolar contributions. The division of the cohesive energy into electrostatic (step 4) and "homolytic" (nonpolar) contributions (step 5) is similar to the Pauling electronegativity definition for diatomic gases; however, the extended Born model is valid for any solids, liquids, and gases. Relative atomic sizes, coordination numbers, and specific lattice symmetry are implicitly included via specific formation energies (step 1) and contributions to the cohesive energy (steps 4 and 5). The box below the thermodynamic cycle depicts the possible range of energies in each step, normalized per mol of atoms. The given range covers all elements, alloys, and inorganic and organic compounds across the periodic table (data from refs[8,51,53,56]).

acid−base properties, chemical reactivity, and any other available experimental physical and chemical data that have a relation to polarity. The extended Born model can be applied to compounds across the periodic table in all aggregate states. Unlike electronegativity, it is not limited to diatomic molecules in the gas phase and therefore broader in coverage.[7]

For a given compound, reproducible atomic charges can be obtained using multiple independent estimates according to these experimental and theoretical sources, including comparisons to chemically similar compounds, and the range of uncertainty is then less than ±10%.[8,19,20] The uncertainty can be as low as ±1% for molecules with known dipole moments (Figure 1a,b). It is critical to distinguish these atomic charges from quantum-mechanically computed charges, which unfortunately remain subject to large scatter, limited physical interpretation, and easily invalidate classical atomistic simulations if used.[8,11,12]

The following examples illustrate the importance of this statement. Water molecules and simple organic molecules are among the earliest compounds for which partial atomic charges, associated dipole moments, and spatially averaged electron densities were incorporated into classical atomistic force fields for molecular simulations.[17,36,63,64] The atomic charges represent dipole moments, which contribute to cohesive energies, hydrogen bonds, and solvation energies of adjacent molecules that can be reproduced in measurements (Figure 1c,d). The oxygen charges in common SPC and TIP3P water models range from −0.82*e* to −0.84*e* with less than 5% deviation and reproduce the dipole moment of liquid water. In comparison, DFT and other electronic structure methods have computed oxygen charges in water anywhere from −0.17*e* to −1.24*e*.[8,11,19] Correlation with physically meaningful values in the above sense is not feasible. As an example for organic compounds, the charge on the carbonyl carbon atoms in aldehydes and ketones is close to +0.45*e* in multiple force fields (CHARMM, AMBER, PCFF, and OPLS-AA), consistent with $R_2C{=}O$ dipole moments measured in the experiment.[18] In contrast, quantum-mechanically derived charges range from +0.075*e* to +1.36*e*. Again, the correspondence is effectively random. As an example for an inorganic compound, the atomic charge for silicon in silica (SiO_2) and oligomeric silicates is +1.1*e* with ±0.1*e* uncertainty in force fields, which is well supported by carbon as a neighbor in the periodic table and several other arguments (Figure 1e).[8,22,39] Values from quantum mechanics range from +0.5*e* to +3.3*e* for the same compound.[22,24,34] These and many other examples[11,12] show that no matter the position in the periodic table, atomic charges from quantum mechanical methods, and associated dipole moments have little physical relevance, with up to 900% uncertainty for the same compound.[65] In contrast, atomic charges defined in agreement with experimentally verifiable dipole moments as well as with the quantities in the extended Born model are between ±1 and ±10% reproducible and are suitable for predictive atomistic simulations.

The large uncertainties in quantum methods may explain why charge separation in alloys and the significance for a range of alloy properties has not been paid much attention to date.[66,67] This contribution is the first step to clarify and quantify chemical bonding in alloys and introduce chemical detail into atomistic models (Figure 1f). The proposed analysis of chemical bonding and the assignment of atomic charges is based on related experimental data and on the extended Born model to achieve consistency with existing force fields and best performance.[19,21,22,26,34,68]

We assume that the polarity of alloys affects their cohesive energy and the surface adsorption of other compounds (Figure 1f) in the same way as (1) the polarity of water and organic molecules determines their cohesive energy and interactions with other compounds (Figure 1a−d) and (2) the polarity of inorganic solids determines their surface energy and interaction with other compounds (Figure 1e). The application of the same definition of atomic charges that works well for organic and other inorganic compounds to alloys enables simulations in far better accuracy, including bulk and surface properties, as well as compatibility with existing models for solvents, minerals, and biopolymers without the need for additional parameters to simulate interfacial interactions.[19,21,46]

3.2. Relation between Alloy Formation Energy and Polarity. Alloy formation in the form of solid solutions, mixed metallic phases, and intermetallic compounds is qualitatively described by the Hume-Rothery rules.[6,69−75] Many alloys exhibit complex-phase diagrams that remain difficult to explain and predict. Enthalpies of formation have been measured for a wide range of compositions[54,71,72,74−78] and theoretically estimated for binary solutions across the periodic table (Figure

DOI: 10.1021/acs.jpcc.8b01891
J. Phys. Chem. C 2018, 122, 14996−15009

a

Compound	Enthalpy of alloy formation ΔH_f at 298 K (kJ/mol of atoms)
PbZn	+5.5 ±1.2
CuNi	+2 ±1.0
Ni_3C	+1.2 ±1.3
InPb	+1 ±0.1
$PdAu_3$	-8 ±1.0
Cu_3Pt	-10.8±1.1
CrNi	-20 ±1.0
AlFe	-23.5 ±1.6
MoB	-28.7 ±1.0
Al_3Ti	-36.8 ±2.1
CrB_2	-39.8 ±2.3
$AlNi_3$	-41 ±1.0
MnPt	-44 ±1.0
$MoSi_2$	-47.9 ±2.1
$GaZr_2$	-53.4 ±2.1
AlNi	-58.3 ±1.1
GdSi	-75.6 ±2.3
YAu_2	-84.6 ±1.8
AlPt	-94.9 ±2.5
AlRh	-106.3 ±1.6

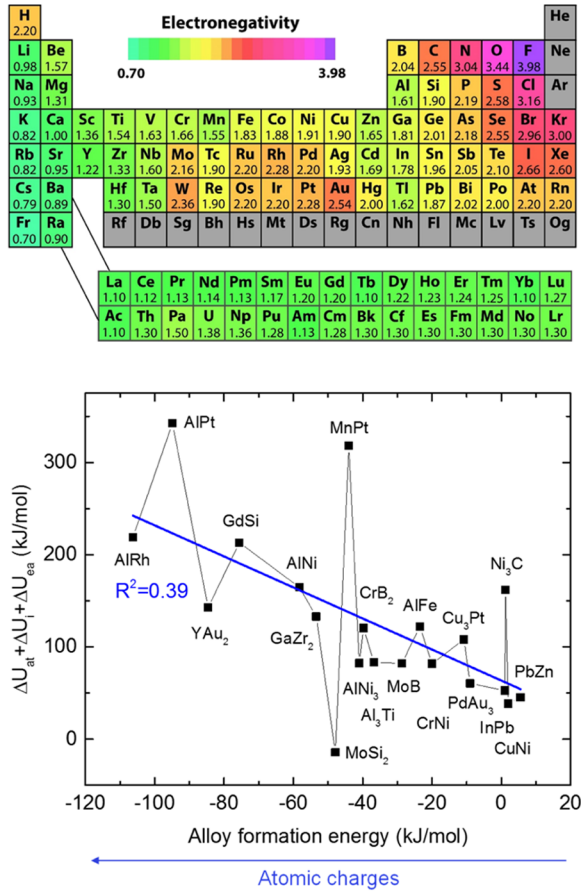

Figure 3. Representative alloy formation enthalpies from experimental measurements and the relation to electronegativity (excluding alkali and earth alkali metals). (a) Examples of energies of formation of binary alloys. Negative values up to −106 kJ/mol indicate up to 25% added cohesion in the alloy compared to the neat metals, primarily because of charge transfer from the more electropositive metal to the more electronegative metal. The given notation places the electron-donating metal to the left and the electron-receiving metal to the right (data from refs[54,72,74,78]). (b) Color-coded periodic table of electronegativity to help illustrate the relationship between charge transfer in the alloy and differences in alloy formation energy (see Figures S2 and S6 for details). (c) Relation of the alloy formation energy to the sum of differences in atomization energy, first ionization energy, and electron affinity of the constituting metals according to the extended Born model (normalized per atom). This quantity correlates with atomic charges for similar coordination environments. Outliers are related to a mismatch in preferred crystal lattice, large differences in cohesive energy, atom size, and electronic structure of the two types of metal atoms.

S1).[69,70] A random selection of values, excluding alloys of alkali and earth alkali metals, is shown in Figure 3. Exothermic values up to about −100 kJ per mol atoms illustrate that stabilization of the alloys relative to the neat metals can be very significant (Figure 3a). The reason is charge transfer and Coulomb attraction because of differences in electronegativity (Figures 3b and S2).[6] As an initial measure, electronegativity differences ($\chi_A - \chi_B$) were defined by Pauling to describe bond dissociation energies $E_d(AB)$ between pairs of atoms A and B in the gas phase in electron volts (eV)

$$E_d(AB) = \frac{E_d(AA) + E_d(BB)}{2} + (\chi_A - \chi_B)^2 \quad (1)$$

Thereby, the electronegativity term $(\chi_A - \chi_B)^2$ adds contributions from partially ionic bonding that can be represented by atomic charges.[79] The alloy formation energy correlates statistically significant with the electronegativity difference between two metals, normalized per atom for AB_x stoichiometry (Figures 3b and S2), and slightly better with the more detailed balance of atomization energies, ionization potential, and electron affinities (Figure 3c).

Alloys are, however, not isolated formula units in the gas phase which electronegativity differences would describe. Alloys are solids with specific crystal structures, and the thermodynamic cycle of alloy formation can be described by the extended Born model (Figure 2).[8] The alloy formation energy (step 1) consists of the atomization energy of metals A and B (step 2), charge transfer between atoms A and B to atomic charges of $+xe$ and $-xe$ (step 3), formation of a new alloy lattice with electrostatic energy (step 4), and remaining nonionic cohesion (step 5). The magnitude of atomic charges is affected by all contributions.[8] High atomization energy describes a propensity toward less ionic bonding (Figure S3a), high ionization energy a propensity toward less ionic bonding (Figure S3b), and high electron affinity (if positive values considered) a propensity toward stronger ionic bonding (Figure S3c). The influence of crystal structures and coordination numbers is included in the atomization of the neat metal lattice (step 2) and in the recombination of partially charged atoms in the gas phase to the alloy or intermetallic crystal structure (step 4) (Figures 2 and S4). All tabulated measures (atomization energy, ionization energy, electron affinity, and electronegativity), given as a difference between

DOI: 10.1021/acs.jpcc.8b01891
J. Phys. Chem. C 2018, 122, 14996−15009

the two constituting metals and normalized per atom, indicate the same average trend in ionic character and in alloy formation energy (Figures S5 and S6a,b). The larger the difference, the lower (further below zero) is the alloy formation enthalpy and the higher the expected difference in atomic charges. The difference in the sum of the three main indicators in the extended Born model (atomization energy, ionization energy, and electron affinity) shows the best correlation with the least number of outliers (Figure 3c), followed by the difference in electronegativity and the difference in electron affinity (Figure S6a,b). Differences in preferred crystal structures of the elements (fcc, body-centered cubic, and hexagonal close-packed) also play a significant role (Figure S4).

For example, Cu and Ni have the same fcc crystal structure, about equal electronegativity (Figure 3b), and the formation energy of CuNi is slightly positive (Figure 3a). Al and Pt have the same fcc crystal structure, quite a notable difference in electronegativity (Figure 3b), and the formation energy of AlPt is strongly negative (Figure 3a). The added ionic attraction can amount to as much as 25% of the average atomization energy and is increased for larger difference in electronegativity for most series of binary alloys (Figure S5). Example series that follow this trend in alloy formation energies are (on the order of larger negative alloy formation energy toward zero)

$$\begin{aligned} &\mathrm{AlPt} < \mathrm{AlNi} < \mathrm{AlFe} \\ &\mathrm{AlNi} < \mathrm{CrNi} < \mathrm{CuNi} \\ &\mathrm{YAu_2} < \mathrm{PdAu_3} \\ &\mathrm{GdSi} < \mathrm{MoSi_2} \\ &\mathrm{AlPt} < \mathrm{MnPt} < \mathrm{Cu_3Pt} \end{aligned} \quad (2)$$

A similar electronegativity difference or electron affinity difference results in similar enthalpy of formation, for example, in the series of lanthanide aluminides.[74] The general trend holds well, whereas outliers are also common (Figure 3c). Outliers are likely when structural mismatches occur, such as a preference for different lattices in the pure metals or in the alloy, a very high difference in atomization energies (>300 kJ/mol), large differences in van der Waals radius, or major differences in the electronic structure. When including all metals across the periodic table, therefore, both large negative and large positive alloy formation energies can be found (Figure S1).[69,70] Highest values below zero are usually associated with intermediate differences in electronegativity. Highest values above zero are found for solid solutions of alkali metals, which have very low atomization energies, in metals with high atomization energy (Y, W, Ti, and Ta, see Figure S3a). Then, the loss of nonpolar metallic bonding in the metal of high atomization energy (up to 800 kJ/mol) is greater than the possible gain in cohesion from charge-transfer and partial ionic interactions. Alkali metals still tend to alloy with Au and a few other strongly electronegative metals or with less cohesive metals (ΔU_{at} < 300 kJ/mol). The challenge for realistic simulations using pair potentials is to capture these trends by appropriate atomic charges or otherwise electronically refined models.[45] All-atom force fields take into account relative atomic sizes and atomization energies (or surface energies) of the neat metals in very good agreement with experiment[44,45] so that the addition of atomic charges is technically easy to do and strongly improves simulation outcomes.

3.3. Determination of Atomic Charges by Matching Experimental Alloy Formation Energies. Charge transfer in alloys therefore depends on the local geometry and differences in the sum of energy contributions in the extended Born model (in simplified form: differences in electronegativity). Reproducible atomic charges can be obtained for alloys with known crystal structure and available measurements of alloy formation energies. Simulations of the alloys can be carried out using LJ potentials[9,44] (or LJ potentials with virtual electrons[45,46]) that reproduce bulk and surface properties of the neat metals, and with added atomic charges (Figures 1f and 4).

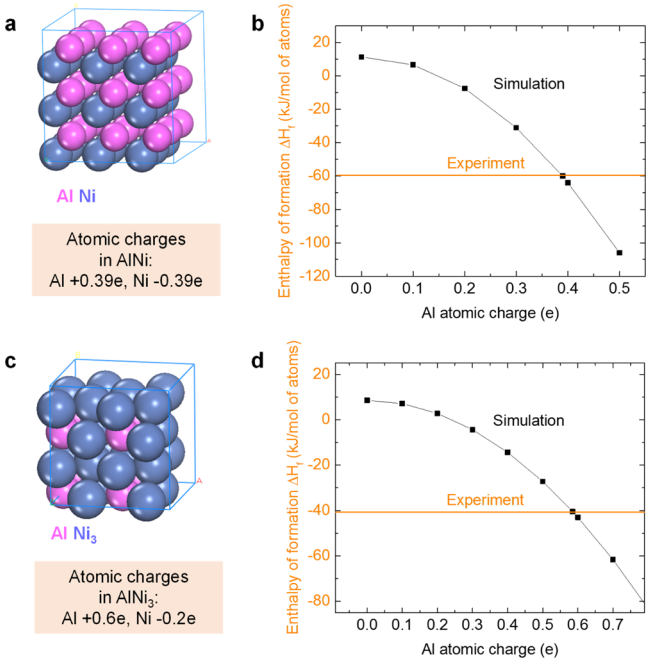

Figure 4. Determination of atomic charges for simulations of Al−Ni alloys using the experimentally reported alloy formation energies. (a) Structure of a 3 × 3 × 3 AlNi supercell. (b) Computed alloy formation energy of AlNi as a function of the atomic charges using simulations with pair potentials for the neat metals (IFF). Atomic charges are chosen such that the computed alloy formation energy matches the experimental value (ref 74). (c) Structure of a 2 × 2 × 2 $AlNi_3$ supercell. (d) Determination of the atomic charges in $AlNi_3$ using the same protocol (ref 77 for formation enthalpy). The magnitude of atomic charges indicates that the alloys are significantly polar solids.

The cohesion of neat metals described by LJ potentials is so strong that the LJ parameters need no modification, or only minor modification, once polarized bonding in alloys is added via atomic charges.

When no charge transfer is assumed in the alloy, that is, when all atomic charges are assumed to be ±0.0*e* as in the neat metals, the alloy formation energy is always positive (steps 3 and 4 in Figure 2 are of zero energy). The reason is that mixtures of metals with inherently different interatomic interactions and surface energies are thermodynamically at least slightly unfavorable unless charge transfer or specific changes in the electronic structure (covalent bonding) create added attraction. For the examples of AlNi and $AlNi_3$ alloys, simulations with LJ parameters for the neat metals show slightly positive enthalpies of alloy formation (Figure 4). The B2 phase of AlNi would show an enthalpy of formation of +12 kJ per mol atoms without charge separation (Figure 4a). The introduction of charges lowers the enthalpy of formation, matching the experimental value of −58 kJ/mol for atomic charges of ±0.39*e*

DOI: 10.1021/acs.jpcc.8b01891
J. Phys. Chem. C 2018, 122, 14996−15009

(Figure 4b). The computed lattice parameter of 2.99 Å (at 0 K) compares reasonably well with the experimental value of 2.89 Å.[52,53] Improvements toward a perfect match can be made using smaller values of σ and ε for Al and Ni in the LJ potential as needed (the charges would then be ~3% higher).[44] Similarly, the $L1_2$ phase of $AlNi_3$ (Figure 4c) shows a positive alloy formation enthalpy of +8.5 kJ/mol if no charge separation is assumed (Figure 4d). The introduction of charges lowers the alloy formation enthalpy and matches the experimental value of −40 kJ/mol for charges of approximately +0.6e for Al and −0.2e for Ni. The lattice parameters in the computation (3.64 Å) and in the experiment (3.57 Å) agree well and could be matched closer if needed.[54] Notably, the atomic charges in both alloys can be represented by the same charge increments of ±0.05e between nearest neighbor Al and Ni atoms even though the alloys have rather different compositions; a small deviation of 2.5% is entirely within the experimental error (±0.04875e for AlNi vs ±0.050e for $AlNi_3$). Using this protocol, the Hamiltonian reproduces structures and energies, including any transitional compositions between the pure metals and the alloys. The assignment of charges is consistent with the extended Born model (Figure 2). For full quantitative detail, positive energy contributions from ionization of the metal (step 3 in Figure 2) could be added and atomic charges may be slightly higher (see Section S1 in the Supporting Information). However, it is difficult to quantify the absolute values of all contributions in the extended Born model by computation and available data (Figure 2), and such modifications are not included in common force fields for organic and inorganic compounds. The simple method outlined here provides a reliable minimum estimate of internal polarity and a large improvement over previous nonpolar alloy models.

Qualitative estimates of the atomic charges can also be made without alloy formation energies using the contributions in the extended Born model in comparison to similar alloys and other polar compounds with known charges (Figures S1 and S3).[8,9] For Al and Ni, as an example, it is seen that Ni atomization energies, ionization energies, and electron affinities have a larger value than those for Al (Table S1). Therefore, Ni is the electronegative component, Al is the electropositive component, and semi-quantitative relations relative to other compounds can be invoked to estimate the charge.[8]

Significant atomic charges on the order of ±0.40e for AlNi and $AlNi_3$ are typical for a broader set of alloys according to known formation energies (Figure 3a) and demonstrate that the alloys are partially ionic solids. The distance between nearest atomic neighbors of ~2.6 Å is larger than common covalent bonds (1.0−1.8 Å).[18] The internal dipoles (product of charge and distance) tend to be larger than that in polar organic compounds and comparable to those in minerals. For example, carbonyl groups in organic molecules ($R_1-(C{=}O)-R_2$ in ketones, amides, and esters) carry atomic charges of ±0.45e at ~1.2 Å distance, and alcohol groups (R_3C-OH) atomic charges of +0.2e and −0.6e on carbon and oxygen atoms at ~1.4 Å distance, respectively.[17,80] The equivalent charges for 2.6 Å bond length in the alloy, leading to the same multipole moment, would be only ±0.21e, or +0.11e and −0.33e, respectively, whereas the actual charges in AlNi of ±0.39e are clearly higher. As another example, silica (SiO_2) contains Si−O bonds of 1.6 Å length and charges of +1.1e and −0.55e.[8] The corresponding charges for a hypothetical bond length of 2.6 Å as found in the alloys are +0.68e and −0.34e, which is comparable to that of $AlNi_3$. A direct measure for the Coulomb attraction in the alloys is also the formation energy. In NiAl alloys, the formation energy is about −60 kJ per mol atoms, on top of metallic bonding (Figure 3a). This energy equals six hydrogen bonds for every atom in the alloy, assuming an average hydrogen bond in water with a strength of −10 kJ per mol atoms and −20 kJ/mol for a pair of atoms (based on the vaporization energy of water of −40.6 kJ/mol that involves two hydrogen bonds and some van der Waals interactions).[18,81,82] This amount of polar bonding is clearly not negligible. Furthermore, NiAl intermetallic compounds are of medium polarity, and some other alloys can exhibit polarized bonding that is twice as strong and may be described as ionic bonding with atomic charges exceeding ±1.0e (Figure 3a).

The partial ionic contributions are thus significant and expected to strongly influence interfacial adhesion of oxides, solvents, organic films, and redox processes on the alloy surface. Experimental data for alloy formation energies, used to derive the atomic charges, are readily available for many alloys and solid solutions,[72,74−78] as well as extensive theoretical data (a selection is shown in Figures 3a and in S1).[69,70] The reliability is high, with typical uncertainties <2 kJ/mol in a common range of 0−100 kJ/mol, so that atomic charges can be derived with uncertainties <10% and <0.05e. Atoms in the top atomic layer of alloy surfaces may thereby exhibit slightly reduced atomic charges because of lower coordination numbers.

It is also noteworthy again that DFT calculations are not recommended to validate internal polarity and atomic charges, or only qualitatively so. The assumptions in the calculation of the electron density and in the partitioning methods result in large scatter.[8,11,12,19] For AlNi, the commonly employed revised PBE functional yields Bader charges of +0.73e for Al and −0.73e for Ni, Mulliken charges of +0.57e for Al and −0.57e for Ni, and Hirshfeld charges of only +0.09e for Al and −0.09e for Ni, all for the same compound (see Section 2). Similarly, for Al and Ni in $AlNi_3$, Bader charges of +1.08e/−0.54e, Mulliken charges of +0.63e/−0.21e, and Hirshfeld charges of +0.09e/−0.03e are obtained. The revised PBE functional for solids (PBEsol) yields about half the Mulliken charges and the same Hirshfeld charges. Despite the wide distribution, the quantum mechanical data qualitatively confirm an important role of polarity. Correlation of the ab initio charges with alloy formation energies, electronegativity differences, and other experimentally observable manifestations of multipole moments is not possible, however. Because of similar limitations, dipole and multipole moments in organic molecules cannot be reproduced (Section 3.1). The uncertainty of DFT methods for atomic charges mainly originates from the choice of the partition method and the basis sets, and the range >500% today remains similar to that 15 years ago.[8] In practice, often the best combination of exchange functionals and basis sets is chosen for a particular problem, and the partition method for the atomic changes accordingly. "Uncertainty" may therefore not be a meaningful term; however, ultimately, there are errors associated with the chosen combination or the determination of which combination is expected to perform well. The use of alloy formation energies from experiment to assign atomic charges in the force field, consistent with the extended Born model, reduces the uncertainty to <10%. DFT methods are nevertheless useful to compute cohesive energies, alloy formation energies, and defect energies in good reliability. Densities, mechanical properties, and surface energies have small to high uncertainties relative to experiment (5, 20, and 50%).[55] The IFF achieves notably better results for surface and

DOI: 10.1021/acs.jpcc.8b01891
J. Phys. Chem. C 2018, 122, 14996−15009

interfacial energies (<5%) and performs similarly well for mechanical properties compared to DFT.[44,46]

3.4. Defect Energies and Charge Distributions. The models for simple and fast simulations of alloy properties based on LJ potentials and atomic charges (CHARMM-IFF) were tested to compute defect energies and explain the distribution of charge at defect sites (Figure 5). The overall quality of results

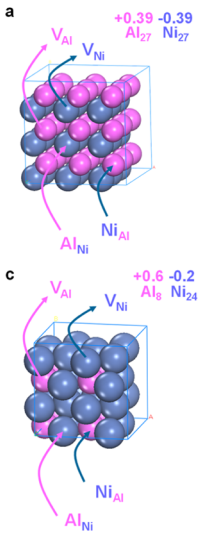

b

Defect type	MM (CHARMM-IFF) (eV)	DFT, rPBE (eV)	EAM (Mishin 2002) (eV)
V_{Ni}	+5.49	+6.51	+5.68
V_{Al}	+5.85	+6.25	+5.65
Al_{Ni} antisite	+3.09	+3.31	+2.92
Ni_{Al} antisite	+2.04*	-0.70	-0.15

d

Defect type	MM (CHARMM-IFF) (eV)	DFT, rPBE (eV)	EAM (Mishin 2004) (eV)
V_{Ni}	+4.97	+7.47	+6.26
V_{Al}	+6.34	+7.32	+6.42
Al_{Ni} antisite	+0.92	+1.16	+0.89
Ni_{Al} antisite	+2.19*	+0.24	+0.78

* See text why the value may be a better match.

Figure 5. Raw defect energies in AlNi and $AlNi_3$ computed by the force field, DFT, and EAM methods. (a) Visualization of an Al vacancy, Ni vacancy, Al antisite, and Ni antisite in an AlNi alloy (B2 phase). (b) Associated raw defect formation energies according to MM simulation with CHARMM-IFF, DFT calculations, and EAM models (from ref 53). (c) Visualization of an Al vacancy, Ni vacancy, Al antisite, and Ni antisite in an $AlNi_3$ alloy ($L1_2$ or γ phase). (d) Associated raw defect formation energies according to MM simulation, DFT calculations, and EAM models (from ref 57). The uncertainty with all models is about ±0.5 eV. The agreement among methods is very good, and associated charge distributions are described in the text.

is the same as with DFT and EAM methods, which are in the same range within approximately ±0.5 eV (see Section 2.2). The calculation of defect energies with the force field necessitates assumptions about the redistribution of the missing charge when a vacancy or antisite is created, and the results are intrinsically linked to modeling the charge distribution. The treatment of defect sites was carried out as previously described for clay, apatite, and cement minerals, as well as for heteroatoms in biomolecules and polymers.[21,34,83,84] Accordingly, the charge left by a missing atom in vacancies is distributed over the first shell of the nearest neighbor atoms, maintaining overall charge neutrality. When different neighbor atoms are present in this coordination shell, the relative distribution of charge is guided by the ionization energies and electron affinities of the neighbor atoms. That is, atoms of higher ionization energies receive less positive charge. These simple rules give consistent results for all defect energies (Figure 5). Moreover, defect energies by DFT can vary up to 1 eV depending on density functional and settings (see Section 2.2), and similar variations have been seen among previously published EAM results and EAM potentials.[53,56,57] Specific defect energies can also be matched by customized charge distributions using the force field, allowing further interpretations. Thereby, odd-looking charge distributions indicate that corresponding energies may not be justified or have another cause (see examples in Table S2).

Very consistent results are obtained for vacancies in AlNi (Figures 5a,b and 6a,b). The missing Ni charge of −0.39*e* in the

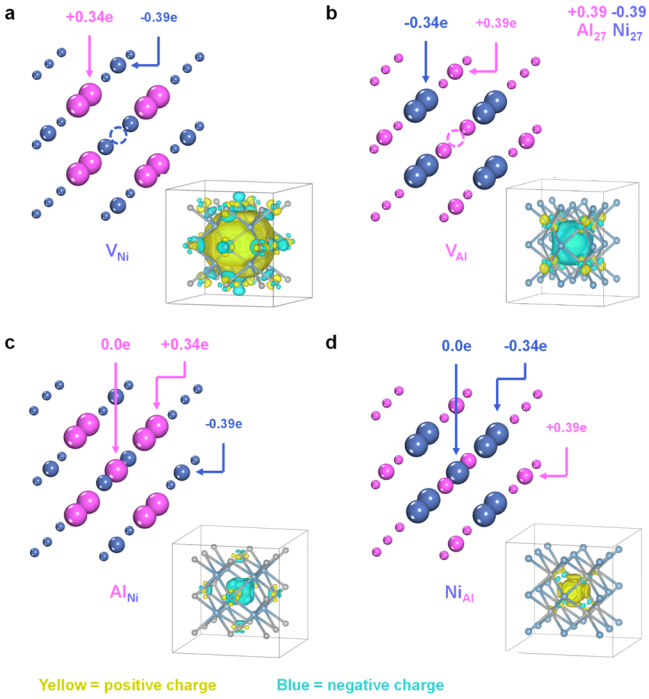

Figure 6. Geometry and charge distribution of defects in AlNi according to atomistic simulations and DFT (insets). (a) Ni vacancy, showing a positive charge from surrounding Al. (b) Al vacancy, showing a negative charge from surrounding Ni. (c) Al antisite, showing a negative charge from the original Ni. (d) Ni antisite, showing a positive charge from the original Al. The difference in local charge at the defect site is mainly accommodated by the first shell of neighbor atoms, consistent with chemical theory and DFT. Evidence for involvement of the second shell of neighbor atoms is weak, and contributions are small (<10% change in atomic charge). Insets show the charge difference map from DFT calculations (alloy minus defect). The isosurface levels for best visualization were chosen as 0.0006, 0.00155, 0.00239, and 0.00239*e*/bohr^3 in (a−d).

Ni vacancy is evenly distributed over the 8 Al neighbors that then have a charge of −0.341*e* (Figure 6a). Analogously, the missing charge of +0.39*e* in the Al vacancy is evenly distributed over the 8 Ni neighbors that then have a charge of +0.341*e* (Figure 6b). The charge distribution after energy minimization with IFF is qualitatively consistent with charge difference maps from DFT calculations for the Ni vacancy and the Al vacancy (insets in Figure 6a,b), and the defect energies match (Figure 5a,b). The Al_{Ni} antisite can be treated the same way as the Ni vacancy with an added Al atom of zero charge that is coordinated only by Al neighbors (Figures 5a,b and 6c). The agreement in defect energies and in charge distribution with DFT and EAM models is also excellent. The same concept further appears justified for the Ni_{Al} antisite, although then DFT and EAM results indicate lower energies than MM (Figures 5a,b and 6d). The differences have no obvious reason. Possibly, through-space delocalization of the negative charge across Ni atoms may stabilize the antisite in DFT, which is not captured by the localized charge distribution in the classical model. The nearest neighbor shell of atoms of the Ni_{Al} antisite consists of Ni atoms only, which reasonably supports a charge

DOI: 10.1021/acs.jpcc.8b01891
J. Phys. Chem. C 2018, 122, 14996−15009

of the incoming Ni atom of ±0.0*e* (Figure 6d). The Ni_{Al} antisite energy in AlNi could be lowered to coincide with DFT and EAM data by increasing the Coulomb attraction in MM (Table S2), for example, the Al atoms in the second neighbor shell could increase their positive charge from +0.39*e* to +0.47*e*, and Ni in the first neighbor shell could increase its negative charge from −0.341*e* to −0.40*e*. Alternatively, the Ni defect could also assume a +0.39*e* positive charge (Ni neighbors retain −0.39*e*), resulting in an energy of the Ni_{Al} antisite of −0.46 eV. These choices appear unsupported unless additional electronic effects play a role, and the second option would also contradict trends in ionization energy and electron affinity. Different electron densities from DFT (insets in Figure 6c,d) qualitatively support the proposed charge distributions in the force field.

Charge distributions in the first neighbor shell also explain defect structures and energies in $AlNi_3$ (Figure 5c,d). In Ni vacancies, the negative Ni charge is distributed over the four nearest positively charged Al atoms, which then have charges of +0.55*e* and Ni remains with −0.20*e* (Figure 7a). The computed

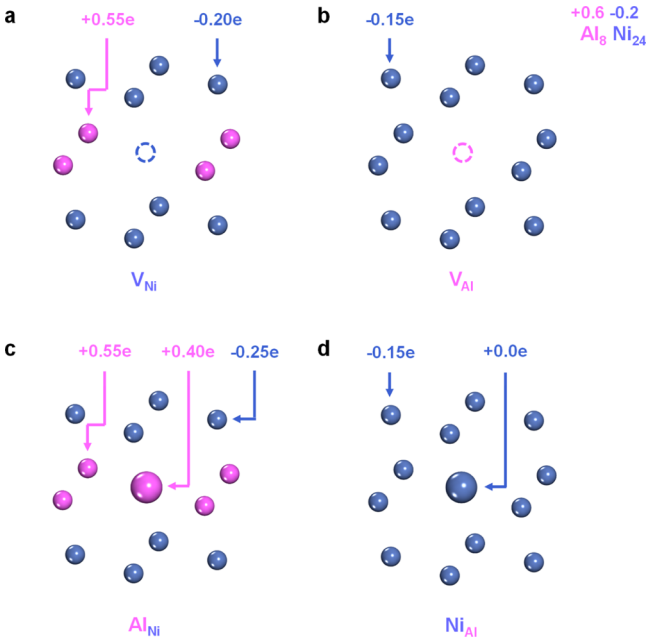

Figure 7. Geometry and charge distribution of defects in $AlNi_3$ in atomistic simulations: (a) Ni vacancy, (b) Al vacancy, (c) Al antisite, and (d) Ni antisite. The difference in local charge at the defect site is primarily accommodated by the first shell of neighbor atoms, and changes in the second shell of neighbor atoms are small (<10% change in atomic charge).

V_{Ni} energy of 4.97 eV is in the right range compared to that of DFT and EAM data, and a better match of 6.03 eV can be achieved when the Al charge is reduced to +0.51*e* and the Ni charge is reduced to −0.18*e* in the first coordination shell (not shown in Figures 5d and in 7a). This example shows that minor changes can have a notable impact. However, it is uncertain that such a charge reduction more in-line with EAM and DFT energies would realistically happen as the alloy composition shifts closer toward AlNi with equal distribution of charges. Distribution of the positive Al charge in Al vacancies (V_{Al}) over the 12 nearest negatively charged Ni atoms yields results in full agreement with DFT and EAM data (Figures 5c,d and 7b). Data for the Al_{Ni} antisite in $AlNi_3$ are also consistent (Figures 5c,d and 7c). The incoming Al atom then enters a coordination environment with both Al and Ni. The negative charge of −0.20*e* from leaving Ni plus +0.6*e* from incoming Al is distributed as −0.8*e* over the neighbors, about 1/2 on positively charged Al and 1/2 on Ni, leading to +0.4*e* on the central Al atom (which has 8 Ni neighbors), +0.55*e* on the four nearest neighbor Al atoms (which have 11 Ni neighbors), and charges of −0.25*e* on surrounding Ni atoms (which have 5 Al neighbors). This defect energy is also sensitive to the charge distribution (Figure 7c). Finally, the Ni_{Al} antisite exhibits a higher energy with IFF compared to DFT and EAM models (Figure 5c,d), whereas the charge distribution appears justified (Figure 7d). The neighbor shell consists of Ni atoms only, which supports a charge of the incoming Ni atom of ±0.0*e* (Figure 7d). The positive charge of the leaving Al atom (+0.6*e*) is evenly spread onto the neighbor shell of 12 Ni atoms (−0.15*e*). To lower the defect energy for a match with DFT values, the Al atoms in the second neighbor shell (not shown) could slightly increase their positive charge and Ni atoms in the first neighbor shell could slightly increase the negative charge. Alternatively, the energy of the Ni_{Al} antisite in $AlNi_3$ would also be reduced to +0.45 eV if the central Ni assumes +0.40*e* charge (and −0.185*e* on Ni neighbors). The lower energy of the Ni_{Al} antisite using DFT could also be a result of through-space charge delocalization among Ni atoms (Figure 7d) that is not captured by the force field.

The results demonstrate that the inclusion of atomic charges in atomistic models of alloys is essential as otherwise the computed defect energies would disagree with EAM and DFT results. The charge created at a defect site distributes over atoms in the first neighbor shell, consistent with maximum energy gains of the neighbor atoms according to ionization potentials and electron affinities. The defect energies are sensitive to fractions of elementary charges, such as approximately ±10%, or ±0.1*e* on defect atoms and ±0.01*e* in coordination shells. Computed defect energies are lower when internal polarity is added by increased opposite charges, or when the charge distribution is spatially further spread out across second shells of neighbor atoms. Computed defect energies are higher when internal polarity is lowered by decreased opposite charges or by a spatially more concentrated charge distribution. Details of charge distributions including second neighbor shells and their effect on energies are given as an example for AlNi in Table S2. It is also noted that calculations with CHARMM-IFF are approximately 10 million times faster than that with DFT and have comparable reliability. It is feasible to test many atomic distributions and analyze systems up to millions of atoms with realistic step edges, crevices, terraces, grain boundaries, and other structural features. These length scales and surface features play an important role for alloy interfacial properties and reactivity,[4] and the models introduced here enable new insights conceptually and computationally.

3.5. Computational Implementation. A simple computational implementation is feasible using charge increments among nearest neighbor atoms. The atomic charges in both AlNi and $AlNi_3$ phases and in all defects can be described with charge increments of ±0.05*e* as a single parameter, which reproduces the experimental alloy formation energies for both alloys. Accordingly, every Al atom increases its positive charge by +0.05*e* for every Ni atom in the nearest coordination shell and by ±0.00*e* for every Al neighbor atom. Equally, every Ni atom increases its negative charge by −0.05*e* for every Al atom in the nearest coordination shell and by ±0.00*e* for every Ni

DOI: 10.1021/acs.jpcc.8b01891
J. Phys. Chem. C 2018, 122, 14996−15009

neighbor atom. This simple protocol reproduces all reported charge distributions (Figures 6 and 7). For example, eight nearest neighbor atoms in AlNi lead to an Al charge of +0.40e with a minor acceptable deviation of 0.01e (see Figure 6b in the presence of a central Al atom). Twelve nearest neighbor atoms in $AlNi_3$ lead to Al and Ni charges of +0.6e/−0.2e (see Figure 7b in the presence of a central Al atom). The charges for all defect sites are also correctly obtained (Figures 6 and 7). The application of such pairwise charge increments to compute atomic charges also preserves overall charge neutrality.

Charge increments are especially helpful to adjust atomic charges in an alloy on the fly during simulations, for example, during defect migration, diffusion, internal nucleation and growth processes, and whenever atomic rearrangements occur. Charges on the individual atoms can be reassigned at any time using charge increments and a distance cutoff for the first shell of neighbor atoms, which is typically well separated from the second coordination shell by about 1 Å. The implementation in simulation codes such as LAMMPS[49] is user-friendly. The only necessary input for a given binary alloy is the accurate determination of the atomic charges by reproducing the experimental alloy formation energy in the simulation for at least one composition (Figure 4), and deriving the applicable charge increment(s).

4. CONCLUSIONS

Major differences in the enthalpy of alloy formation across the periodic table are shown to be associated with polar bonding and charge transfer between the constituting metals. Alloys can be significantly polar, with internal and surface dipoles comparable to organic compounds and minerals. The degree of polarity depends on the coordination geometry and electronegativity difference of the constituent metals and can be quantified by the extended Born model. Atomic charges suitable for classical simulations, and consistent with the definition for other organic and inorganic compounds,[8,19] can be identified from simulations of the alloy using pair potentials for the neat metals so that the computed alloy formation energy matches the available experimental data (and taking into account the contributions by the partial ionization energy as necessary). The atomic charges can be converted into pairwise charge increments and applied to compute the internal charge distribution for different alloy stoichiometries, atomic arrangements, and defects.

These concepts and methods are illustrated for the examples of AlNi and $AlNi_3$. The computed geometry and energies of defects using the polar alloy models are in very good agreement with DFT and EAM simulations, and the agreement necessitates the inclusion of atomic charges. The charge distribution at vacancies and antisites can be described by partitioning of the excess charge onto the first shell of neighbor atoms according to their charge state and electronegativity, maintaining overall electroneutrality. The force-field-based defect energies are sensitive to small changes in charge distribution on the nearest neighbor shell (about ±10%), and similar differences under 1 eV can be observed in DFT calculations upon changes in density functional or energy cutoff, as well as using different EAM potentials.

The use of atomic charges in alloys, consistent with alloy formation energies, opens up new avenues in atomistic simulations of bulk metallic materials and disordered interfaces up to billions of atoms to deliver insights into the internal structure, interfacial assembly, and surface reactivity. The proposed models have much faster speed than density functional methods and are of comparable accuracy. Extensions for chemical reactions[42,68,85,86] and electrode potentials[46] can be applied as shown for pure metals previously.

Potential applications include insights into crystal growth, interfacial assembly, and reaction mechanisms in catalysis and corrosion. Local differences in charge distribution have major impacts on the internal structure and defects, and a significant influence can be expected for interfacial interactions with organic compounds, coatings, biomacromolecules, solvents, oxides, hydroxides, and gases.[21] In particular, polarized bonding is likely to play a role in the activity of alloy catalysts and electrocatalysts. The polar alloy models can be used in combination with quantum mechanical methods and experimental data to gain more accurate insights into reactions in the vicinity of alloy surfaces,[31] including binding modes and changes in the electronic structure, charge transfer and formation of oxides, and monitoring defective and disordered interfaces up to the micrometer scale.[87,88] Looking forward, the methods reported here could also be directly coupled with atomic electron tomography,[89] which can experimentally determine the three-dimensional coordinates of atoms in materials including point defects and chemical disorder with high precision[90] to understand the structure−property relationships of materials at the single-atom level.

■ ASSOCIATED CONTENT

Supporting Information

The Supporting Information is available free of charge on the ACS Publications website at DOI: 10.1021/acs.jpcc.8b01891.

Examples of approximate enthalpies of solution of liquid metals; Pauling electronegativity of the elements; periodic tables of atomization energy, first ionization energy, and electron affinity; periodic table of metal crystal structures; examples of the enthalpy of alloy formation according to experimental measurements; correlation of the energy of alloy formation with properties in the extended Born model; oscillations of the computed electron density of Ni using VASP; determination of atomic charges in Al-Ni alloys using the Extended Born model; influence of various alternative charge distributions in AlNi on the defect formation energies; and details of the quantitative evaluation of the extended Born model for alloys (PDF)

■ AUTHOR INFORMATION

Corresponding Author

*E-mail: hendrik.heinz@colorado.edu.

ORCID

Yu Huang: 0000-0003-1793-0741

James M. Rondinelli: 0000-0003-0508-2175

Hendrik Heinz: 0000-0002-6776-7404

Notes

The authors declare no competing financial interest.

■ ACKNOWLEDGMENTS

This work was supported by the Office of Naval Research (ONR-MURI-N00014-14-1-0675 and N00014-16-1-2280), the National Science Foundation (DMREF 1623947 and CBET 1530790), and the University of Colorado at Boulder. The allocation of computational resources at the CU Biofrontiers

DOI: 10.1021/acs.jpcc.8b01891
J. Phys. Chem. C 2018, 122, 14996−15009

Computing Cluster and at the Ohio Supercomputing Center is acknowledged. This work further used resources of the Oak Ridge Leadership Computing Facility at the Oak Ridge National Laboratory, which is supported by the Office of Science of the U.S. Department of Energy under Contract No. DE-AC05-00OR22725, the Argonne Leadership Computing Facility, which is a DOE Office of Science User Facility supported under Contract DE-AC02-06CH11357, and the Janus supercomputer, which is supported by the National Science Foundation (award number CNS-0821794).

REFERENCES

(1) Kim, S. I.; Lee, K. H.; Mun, H. A.; Kim, H. S.; Hwang, S. W.; Roh, J. W.; Yang, D. J.; Shin, W. H.; Li, X. S.; Lee, Y. H.; et al. Dense Dislocation Arrays Embedded in Grain Boundaries for High-Performance Bulk Thermoelectrics. *Science* **2015**, *348*, 109−114.

(2) Wang, D.; Xin, H. L.; Hovden, R.; Wang, H.; Yu, Y.; Muller, D. A.; DiSalvo, F. J.; Abruña, H. D. Structurally Ordered Intermetallic Platinum-Cobalt Core-Shell Nanoparticles with Enhanced Activity and Stability as Oxygen Reduction Electrocatalysts. *Nat. Mater.* **2013**, *12*, 81−87.

(3) King, A. D.; Birbilis, N.; Scully, J. R. Accurate Electrochemical Measurement of Magnesium Corrosion Rates; a Combined Impedance, Mass-Loss and Hydrogen Collection Study. *Electrochim. Acta* **2014**, *121*, 394−406.

(4) Ai, J.-H.; Ha, H. M.; Gangloff, R. P.; Scully, J. R. Hydrogen Diffusion and Trapping in a Precipitation-Hardened Nickel-Copper-Aluminum Alloy Monel K-500 (UNS N05500). *Acta Mater.* **2013**, *61*, 3186−3199.

(5) Perepezko, J. H.; Imhoff, S. D.; Chen, M.-W.; Wang, J.-Q.; Gonzalez, S. Nucleation of Shear Bands in Amorphous Alloys. *Proc. Natl. Acad. Sci. U.S.A.* **2014**, *111*, 3938−3942.

(6) Miedema, A. R.; de Boer, F. R.; de Chatel, P. F. Empirical Description of the Role of Electronegativity in Alloy Formation. *J. Phys. F: Met. Phys.* **1973**, *3*, 1558−1576.

(7) Pauling, L. *The Nature of the Chemical Bond and the Structure of Molecules and Crystals: An Introduction to Modern Structural Chemistry*, 3rd ed.; Cornell University Press: Ithaca, NY, 1960.

(8) Heinz, H.; Suter, U. W. Atomic Charges for Classical Simulations of Polar Systems. *J. Phys. Chem. B* **2004**, *108*, 18341−18352.

(9) Heinz, H.; Farmer, B. L.; Pandey, R. B.; Slocik, J. M.; Patnaik, S. S.; Pachter, R.; Naik, R. R. Nature of Molecular Interactions of Peptides with Gold, Palladium, and Pd-Au Bimetal Surfaces in Aqueous Solution. *J. Am. Chem. Soc.* **2009**, *131*, 9704−9714.

(10) Daw, M. S.; Foiles, S. M.; Baskes, M. I. The Embedded-Atom Method: A Review of Theory and Applications. *Mater. Sci. Rep.* **1993**, *9*, 251−310.

(11) Gross, K. C.; Seybold, P. G.; Hadad, C. M. Comparison of Different Atomic Charge Schemes for Predicting pKa Variations in Substituted Anilines and Phenols. *Int. J. Quantum Chem.* **2002**, *90*, 445−458.

(12) Wang, B.; Li, S. L.; Truhlar, D. G. Modeling the Partial Atomic Charges in Inorganometallic Molecules and Solids and Charge Redistribution in Lithium-Ion Cathodes. *J. Chem. Theory Comput.* **2014**, *10*, 5640−5650.

(13) Pernpointner, M.; Seth, M.; Schwerdtfeger, P. A Point-Charge Model for the Nuclear Quadrupole Moment: Coupled-Cluster, Dirac-Fock, Douglas-Kroll, and Nonrelativistic Hartree-Fock Calculations for the Cu and F Electric Field Gradients in CuF. *J. Chem. Phys.* **1998**, *108*, 6722−6738.

(14) White, B. R.; Wagner, C. R.; Truhlar, D. G.; Amin, E. A. Molecular Modeling of Geometries, Charge Distributions, and Binding Energies of Small, Druglike Molecules Containing Nitrogen Heterocycles and Exocyclic Amino Groups in the Gas Phase and in Aqueous Solution. *J. Chem. Theory Comput.* **2008**, *4*, 1718−1732.

(15) Wang, B.; Li, S. L.; Truhlar, D. G. Modeling the Partial Atomic Charges in Inorganometallic Molecules and Solids and Charge Redistribution in Lithium-Ion Cathodes. *J. Chem. Theory Comput.* **2014**, *10*, 5640−5650.

(16) Mahoney, M. W.; Jorgensen, W. L. A Five-Site Model for Liquid Water and the Reproduction of the Density Anomaly by Rigid, Nonpolarizable Potential Functions. *J. Chem. Phys.* **2000**, *112*, 8910−8922.

(17) MacKerell, A. D., Jr.; Bashford, D.; Bellott, M.; Dunbrack, R. L., Jr.; Evanseck, J. D.; Fields, M. J.; Fischer, S.; Gao, J.; Guo, H.; Ha, S.; et al. All-Atom Empirical Potential for Molecular Modeling and Dynamics Studies of Proteins. *J. Phys. Chem. B* **1998**, *102*, 3586−3616.

(18) Lide, D. R. *CRC Handbook of Chemistry and Physics*, 96th ed.; CRC Press: Boca Raton, FL, 2015.

(19) Heinz, H.; Lin, T.-J.; Mishra, R. K.; Emami, F. S. Thermodynamically Consistent Force Fields for the Assembly of Inorganic, Organic, and Biological Nanostructures: The Interface Force Field. *Langmuir* **2013**, *29*, 1754−1765.

(20) Dharmawardhana, C. C.; Kanhaiya, K.; Lin, T.-J.; Garley, A.; Knecht, M. R.; Zhou, J.; Miao, J.; Heinz, H. Reliable Computational Design of Biological-Inorganic Materials to the Large Nanometer Scale Using Interface-FF. *Mol. Simul.* **2017**, *43*, 1394−1405.

(21) Heinz, H.; Ramezani-Dakhel, H. Simulations of Inorganic−Bioorganic Interfaces to Discover New Materials: Insights, Comparisons to Experiment, Challenges, and Opportunities. *Chem. Soc. Rev.* **2016**, *45*, 412−448.

(22) Emami, F. S.; Puddu, V.; Berry, R. J.; Varshney, V.; Patwardhan, S. V.; Perry, C. C.; Heinz, H. Force Field and a Surface Model Database for Silica to Simulate Interfacial Properties in Atomic Resolution. *Chem. Mater.* **2014**, *26*, 2647−2658.

(23) Lin, T.-J.; Heinz, H. Accurate Force Field Parameters and pH Resolved Surface Models for Hydroxyapatite to Understand Structure, Mechanics, Hydration, and Biological Interfaces. *J. Phys. Chem. C* **2016**, *120*, 4975−4992.

(24) Mishra, R. K.; Flatt, R. J.; Heinz, H. Force Field for Tricalcium Silicate and Insight into Nanoscale Properties: Cleavage, Initial Hydration, and Adsorption of Organic Molecules. *J. Phys. Chem. C* **2013**, *117*, 10417−10432.

(25) Mishra, R. K.; Fernández-Carrasco, L.; Flatt, R. J.; Heinz, H. A Force Field for Tricalcium Aluminate to Characterize Surface Properties, Initial Hydration, and Organically Modified Interfaces in Atomic Resolution. *Dalton Trans.* **2014**, 10602−10616.

(26) Mishra, R. K.; Mohamed, A. K.; Geissbühler, D.; Manzano, H.; Jamil, T.; Shahsavari, R.; Kalinichev, A. G.; Galmarini, S.; Tao, L.; Heinz, H.; et al. CEMFF: A Force Field Database for Cementitious Materials Including Validations, Applications and Opportunities. *Cem. Concr. Res.* **2017**, *102*, 68−89.

(27) Somorjai, G. A.; Li, Y. Impact of Surface Chemistry. *Proc. Natl. Acad. Sci. U.S.A.* **2011**, *108*, 917−924.

(28) Gorr, B.; Wang, L.; Burk, S.; Azim, M.; Majumdar, S.; Christ, H.-J.; Mukherji, D.; Rösler, J.; Schliephake, D.; Heilmaier, M. High-Temperature Oxidation Behavior of Mo-Si-B-Based and Co-Re-Cr-Based Alloys. *Intermetallics* **2014**, *48*, 34−43.

(29) Zhao, Z.; Feng, M.; Zhou, J.; Liu, Z.; Li, M.; Fan, Z.; Tsen, O.; Miao, J.; Duan, X.; Huang, Y. Composition Tunable Ternary Pt-Ni-Co Octahedra for Optimized Oxygen Reduction Activity. *Chem. Commun.* **2016**, *52*, 11215−11218.

(30) Huang, X.; Zhao, Z.; Cao, L.; Chen, Y.; Zhu, E.; Lin, Z.; Li, M.; Yan, A.; Zettl, A.; Wang, Y. M.; et al. High-Performance Transition Metal-Doped Pt3Ni Octahedra for Oxygen Reduction Reaction. *Science* **2015**, *348*, 1230−1234.

(31) Smith, M. B. *March's Advanced Organic Chemistry: Reactions, Mechanisms, and Structure*, 7th ed.; Wiley: Hoboken, NJ, 2012.

(32) Jorgensen, W. L.; Maxwell, D. S.; Tirado-Rives, J. Development and Testing of the OPLS All-Atom Force Field on Conformational Energetics and Properties of Organic Liquids. *J. Am. Chem. Soc.* **1996**, *118*, 11225−11236.

(33) Wang, J. M.; Wolf, R. M.; Caldwell, J. W.; Kollman, P. A.; Case, D. A. Development and Testing of a General Amber Force Field. *J. Comput. Chem.* **2004**, *25*, 1157−1174.

DOI: 10.1021/acs.jpcc.8b01891
J. Phys. Chem. C 2018, 122, 14996−15009

(34) Heinz, H.; Koerner, H.; Anderson, K. L.; Vaia, R. A.; Farmer, B. L. Force Field for Mica-Type Silicates and Dynamics of Octadecylammonium Chains Grafted to Montmorillonite. *Chem. Mater.* **2005**, *17*, 5658−5669.
(35) Born, M. Eine Thermochemische Anwendung Der Gittertheorie. *Verh. Dtsch. Phys. Ges.* **1919**, *21*, 13−24.
(36) Dauber-Osguthorpe, P.; Roberts, V. A.; Osguthorpe, D. J.; Wolff, J.; Genest, M.; Hagler, A. T. Structure and Energetics of Ligand Binding to Proteins: Escherichia Coli Dihydrofolate Reductase-Trimethoprim, a Drug-Receptor System. *Proteins: Struct., Funct., Genet.* **1988**, *4*, 31−47.
(37) Pronk, S.; Páll, S.; Schulz, R.; Larsson, P.; Bjelkmar, P.; Apostolov, R.; Shirts, M. R.; Smith, J. C.; Kasson, P. M.; van der Spoel, D.; et al. Gromacs 4.5: A High-Throughput and Highly Parallel Open Source Molecular Simulation Toolkit. *Bioinformatics* **2013**, *29*, 845−854.
(38) Pramanik, C.; Gissinger, J. R.; Kumar, S.; Heinz, H. Carbon Nanotube Dispersion in Solvents and Polymer Solutions: Mechanisms, Assembly, and Preferences. *ACS Nano* **2017**, *11*, 12805−12816.
(39) Heinz, H.; Castelijns, H. J.; Suter, U. W. Structure and Phase Transitions of Alkyl Chains on Mica. *J. Am. Chem. Soc.* **2003**, *125*, 9500−9510.
(40) Nicolosi, V.; Chhowalla, M.; Kanatzidis, M. G.; Strano, M. S.; Coleman, J. N. Liquid Exfoliation of Layered Materials. *Science* **2013**, *340*, 1226419.
(41) Ramezani-Dakhel, H.; Mirau, P. A.; Naik, R. R.; Knecht, M. R.; Heinz, H. Stability, Surface Features, and Atom Leaching of Palladium Nanoparticles: Toward Prediction of Catalytic Functionality. *Phys. Chem. Chem. Phys.* **2013**, *15*, 5488−5492.
(42) Ramezani-Dakhel, H.; Bedford, N. M.; Woehl, T. J.; Knecht, M. R.; Naik, R. R.; Heinz, H. Nature of Peptide Wrapping onto Metal Nanoparticle Catalysts and Driving Forces for Size Control. *Nanoscale* **2017**, *9*, 8401−8409.
(43) Fu, Y.-T.; Zartman, G. D.; Yoonessi, M.; Drummy, L. F.; Heinz, H. Bending of Layered Silicates on the Nanometer Scale: Mechanism, Stored Energy, and Curvature Limits. *J. Phys. Chem. C* **2011**, *115*, 22292−22300.
(44) Heinz, H.; Vaia, R. A.; Farmer, B. L.; Naik, R. R. Accurate Simulation of Surfaces and Interfaces of Face-Centered Cubic Metals Using 12-6 and 9-6 Lennard-Jones Potentials. *J. Phys. Chem. C* **2008**, *112*, 17281−17290.
(45) Xu, R.; Chen, C.-C.; Wu, L.; Scott, M. C.; Theis, W.; Ophus, C.; Bartels, M.; Yang, Y.; Ramezani-Dakhel, H.; Sawaya, M. R.; et al. Three-Dimensional Coordinates of Individual Atoms in Materials Revealed by Electron Tomography. *Nat. Mater.* **2015**, *14*, 1099−1103.
(46) Geada, I. L.; Ramezani-Dakhel, H.; Jamil, T.; Sulpizi, M.; Heinz, H. Insight into Induced Charges at Metal Surfaces and Biointerfaces Using a Polarizable Lennard-Jones Potential. *Nat. Commun.* **2018**, *9*, 716.
(47) Gupta, A.; Boekfa, B.; Sakurai, H.; Ehara, M.; Priyakumar, U. D. Structure, Interaction, and Dynamics of Au/Pd Bimetallic Nanoalloys Dispersed in Aqueous Ethylpyrrolidone, a Monomeric Moiety of Polyvinylpyrrolidone. *J. Phys. Chem. C* **2016**, *120*, 17454−17464.
(48) *Materials Studio 7.0 Program Suite and User Guide*; Biovia/Accelrys, Inc.: Cambridge, U.K., 2015.
(49) Plimpton, S. Fast Parallel Algorithms for Short-Range Molecular Dynamics. *J. Comput. Phys.* **1995**, *117*, 1−19.
(50) Kresse, G.; Furthmüller, J. Efficiency of Ab Initio Total Energy Calculations for Metals and Semiconductors Using a Plane-Wave Basis Set. *Comput. Mater. Sci.* **1996**, *6*, 15−50.
(51) Freysoldt, C.; Grabowski, B.; Hickel, T.; Neugebauer, J.; Kresse, G.; Janotti, A.; Van de Walle, C. G. First-Principles Calculations for Point Defects in Solids. *Rev. Mod. Phys.* **2014**, *86*, 253−305.
(52) Kittel, C. *Introduction to Solid State Physics*; Wiley Interscience: New York, 1986.
(53) Mishin, Y.; Mehl, M. J.; Papaconstantopoulos, D. A. Embedded-Atom Potential for B2-Nial. *Phys. Rev. B: Condens. Matter Mater. Phys.* **2002**, *65*, 224114.
(54) Foiles, S. M.; Daw, M. S. Application of the Embedded Atom Method to Ni_3Al. *J. Mater. Res.* **1987**, *2*, 5−15.
(55) Singh-Miller, N. E.; Marzari, N. Surface Energies, Work Functions, and Surface Relaxations of Low-Index Metallic Surfaces from First Principles. *Phys. Rev. B: Condens. Matter Mater. Phys.* **2009**, *80*, 235407.
(56) Mishin, Y.; Farkas, D. Atomistic Simulation of Point Defects and Diffusion in B2 Nial .1. Point Defect Energetics. *Philos. Mag.* **1997**, *75*, 169−185.
(57) Mishin, Y. Atomistic Modeling of the Gamma and Gamma '-Phases of the Ni-Al System. *Acta Mater.* **2004**, *52*, 1451−1467.
(58) Kresse, G.; Hafner, J. Ab Initio Molecular Dynamics for Liquid Metals. *Phys. Rev. B: Condens. Matter Mater. Phys.* **1993**, *47*, 558−561.
(59) Kresse, G.; Hafner, J. Ab Initio Molecular Dynamics Simulation of the Liquid-Metal-Amorphous-Semiconductor Transition in Germanium. *Phys. Rev. B: Condens. Matter Mater. Phys.* **1994**, *49*, 14251−14269.
(60) Kresse, G.; Furthmüller, J. Efficient Iterative Schemes for Ab Initio Total-Energy Calculations Using a Plane-Wave Basis Set. *Phys. Rev. B: Condens. Matter Mater. Phys.* **1996**, *54*, 11169−11186.
(61) Perdew, J. P.; Burke, K.; Ernzerhof, M. Generalized Gradient Approximation Made Simple. *Phys. Rev. Lett.* **1996**, *77*, 3865−3868.
(62) Perdew, J. P.; Burke, K.; Ernzerhof, M. Erratum: Generalized Gradient Approximation Made Simple. *Phys. Rev. Lett.* **1997**, *78*, 1396.
(63) Berendsen, H. J. C.; Grigera, J. R.; Straatsma, T. P. The Missing Term in Effective Pair Potentials. *J. Phys. Chem.* **1987**, *91*, 6269−6271.
(64) Stillinger, F. H.; Rahman, A. Improved Simulation of Liquid Water by Molecular Dynamics. *J. Chem. Phys.* **1974**, *60*, 1545−1557.
(65) Ritchie, J. P.; Bachrach, S. M. Some Methods and Applications of Electron Density Distribution Analysis. *J. Comput. Chem.* **1987**, *8*, 499−509.
(66) Li, M.; Zhao, Z.; Cheng, T.; Fortunelli, A.; Chen, C.-Y.; Yu, R.; Zhang, Q.; Gu, L.; Merinov, B. V.; Lin, Z.; et al. Ultrafine Jagged Platinum Nanowires Enable Ultrahigh Mass Activity for the Oxygen Reduction Reaction. *Science* **2016**, *354*, 1414−1419.
(67) Mueller, T. Ab Initio Determination of Structure-Property Relationships in Alloy Nanoparticles. *Phys. Rev. B: Condens. Matter Mater. Phys.* **2012**, *86*, 144201.
(68) Bedford, N. M.; Ramezani-Dakhel, H.; Slocik, J. M.; Briggs, B. D.; Ren, Y.; Frenkel, A. I.; Petkov, V.; Heinz, H.; Naik, R. R.; Knecht, M. R. Elucidation of Peptide-Directed Palladium Surface Structure for Biologically Tunable Nanocatalysts. *ACS Nano* **2015**, *9*, 5082−5092.
(69) Miedema, A. R.; de Boer, F. R.; Boom, R. Model Predictions for the Enthalpy of Formation of Transition Metal Alloys. *Calphad* **1977**, *1*, 341−359.
(70) Niessen, A. K.; de Boer, F. R.; Boom, R.; de Châtel, P. F.; Mattens, W. C. M.; Miedema, A. R. Model Predictions for the Enthalpy of Formation of Transition Metal Alloys II. *Calphad* **1983**, *7*, 51−70.
(71) De Boer, F. R.; Boom, R.; Mattens, W. C. M.; Miedema, A. R.; Niessen, A. K. *Cohesion in Metals—Transition Metal Alloys*; Elsevier: Amsterdam, 1989.
(72) Meschel, S. V.; Kleppa, O. J. Standard Enthalpies of Formation of 4d Aluminides by Direct Synthesis Calorimetry. *J. Alloys Compd.* **1993**, *191*, 111−116.
(73) *Cost 507: Thermochemical Database for Light Metal Alloys*; European Communities: Brussels, 1998.
(74) Meschel, S. V.; Kleppa, O. J. Thermochemistry of Alloys of Transition Metals and Lanthanide Metals with Some Iiib and Ivb Elements in the Periodic Table. *J. Alloys Compd.* **2001**, *321*, 183−200.
(75) Meschel, S. V.; Kleppa, O. J. Thermochemistry of Some Binary Alloys of Noble Metals (Cu, Ag, Au) and Transition Metals by High Temperature Direct Synthesis Calorimetry. *J. Alloys Compd.* **2003**, *350*, 205−212.
(76) Desai, P. D. Thermodynamic Properties of Selected Binary Aluminum Alloy Systems. *J. Phys. Chem. Ref. Data* **1987**, *16*, 109−124.
(77) Rzyman, K.; Moser, Z. Enthalpies of Formation of Ni3Al: Experiment Versus Theory. *J. Phase Equilib.* **1996**, *17*, 173−178.

DOI: 10.1021/acs.jpcc.8b01891
J. Phys. Chem. C 2018, 122, 14996−15009

(78) Hultgren, R.; Desai, P. D.; Hawkins, D. T.; Gleiser, M.; Kelley, K. K. *Selected Values of Thermodynamic Properties of Alloys*; American Society for Metals: Metals Park, Ohio, 1973.
(79) Huheey, J. E.; Keiter, E. A.; Keiter, R. L. *Inorganic Chemistry—Principles of Structure and Reactivity*, 4th ed.; Harper Collins College Publishers: New York, 1993.
(80) Sun, H.; Mumby, S. J.; Maple, J. R.; Hagler, A. T. An Ab-Initio CFF93 All-Atom Force Field for Polycarbonates. *J. Am. Chem. Soc.* **1994**, *116*, 2978−2987.
(81) Sheu, S.-Y.; Yang, D.-Y.; Selzle, H. L.; Schlag, E. W. Energetics of Hydrogen Bonds in Peptides. *Proc. Natl. Acad. Sci. U.S.A.* **2003**, *100*, 12683−12687.
(82) Patwardhan, S. V.; Emami, F. S.; Berry, R. J.; Jones, S. E.; Naik, R. R.; Deschaume, O.; Heinz, H.; Perry, C. C. Chemistry of Aqueous Silica Nanoparticle Surfaces and the Mechanism of Selective Peptide Adsorption. *J. Am. Chem. Soc.* **2012**, *134*, 6244−6256.
(83) Heinz, H.; Paul, W.; Suter, U. W.; Binder, K. Analysis of the Phase Transitions in Alkyl-Mica by Density and Pressure Profiles. *J. Chem. Phys.* **2004**, *120*, 3847−3854.
(84) Huang, J.; MacKerell, A. D. Charmm36 All-Atom Additive Protein Force Field: Validation Based on Comparison to NMR Data. *J. Comput. Chem.* **2013**, *34*, 2135−2145.
(85) Coppage, R.; Slocik, J. M.; Ramezani-Dakhel, H.; Bedford, N. M.; Heinz, H.; Naik, R. R.; Knecht, M. R. Exploiting Localized Surface Binding Effects to Enhance the Catalytic Reactivity of Peptide-Capped Nanoparticles. *J. Am. Chem. Soc.* **2013**, *135*, 11048−11054.
(86) Heinz, H.; Vaia, R. A.; Koerner, H.; Farmer, B. L. Photoisomerization of Azobenzene Grafted to Layered Silicates: Simulation and Experimental Challenges. *Chem. Mater.* **2008**, *20*, 6444−6456.
(87) Volders, C.; Monazami, E.; Ramalingam, G.; Reinke, P. Alternative Route to Silicene Synthesis Via Surface Reconstruction on H-MoSi2 Crystallites. *Nano Lett.* **2017**, *17*, 299−307.
(88) Ramanathan, R.; Ramalingam, G.; Perepezko, J. H.; Reinke, P.; Voorhees, P. W. Evolution of NiO Island Size Distributions During the Oxidation of a Ni-5Cr Alloy: Experiment and Modeling. *ACS Appl. Mater. Interfaces* **2018**, *10*, 9136−9146.
(89) Miao, J.; Ercius, P.; Billinge, S. J. L. Atomic Electron Tomography: 3D Structures without Crystals. *Science* **2016**, *353*, aaf2157.
(90) Yang, Y.; et al. Deciphering Chemical Order/Disorder and Material Properties at the Single-Atom Level. *Nature* **2017**, *542*, 75−79.

DOI: 10.1021/acs.jpcc.8b01891
J. Phys. Chem. C 2018, 122, 14996−15009